

Correction of artefacts in optical projection tomography

Johnathon R Walls¹, John G Sled¹, James Sharpe²
and R Mark Henkelman¹

¹ Mouse Imaging Centre, Hospital for Sick Children, University of Toronto,
555 University Avenue, Toronto, Ontario M5G 1X8, Canada

² MRC Human Genetics Unit, Western General Hospital, Crewe Road South, EH4 2XU, UK

E-mail: johnathon.walls@utoronto.ca

Received 24 March 2005, in final form 2 June 2005

Published 21 September 2005

Online at stacks.iop.org/PMB/50/4645

Abstract

A new imaging technique called optical projection tomography (OPT), essentially an optical version of x-ray computed tomography (CT), provides molecular specificity, cellular resolution and larger specimen coverage (≈ 1 cubic centimetre) than was previously possible with other imaging techniques. It is ideally suited to gene expression studies in small animals. Reconstructed OPT images demonstrate several artefacts which reduce the overall image quality. In this paper, we describe methods to prevent smear artefacts due to illumination intensity fluctuation, ring artefacts due to CCD pixel sensitivity variation and a new 'detector edge' artefact caused by non-zero background signal. We also present an automated method to align the position of the rotational axis during image reconstruction. Finally, we propose a method to eliminate bowl artefacts due to projection truncation using a lower resolution OPT scan of the same specimen. This solution also provides OPT with the ability to obtain a high-resolution reconstruction from a region of interest of a specimen that is larger than the field of view. Implementation of these corrections and modifications increases the accuracy of the OPT imaging technique and extends its capabilities to obtain higher resolution data from within a whole specimen.

1. Introduction

The advent of genetic research using animal models has driven the demand for three-dimensional biological imaging of small specimens. The ability to visualize organs and whole organisms in 3D leads to a better understanding of development. 3D imaging also enables mapping of the time and location of gene expression leading to an understanding of developmental genetics.

Many clinical imaging techniques have been adapted in order to obtain high-resolution 3D images for the study of animals such as mice, chicks, fish or rats. Adaptation of clinical x-ray computed tomography (CT) has led to μ CT (Flannery *et al* 1987). MR microscopy uses higher magnetic fields and is able to sample at high resolution with excellent soft tissue contrast (Johnson *et al* 2002). Ultrasound has been scaled to high resolution using higher frequency sound waves in order to decrease the wavelength (Foster *et al* 2000). PET has been scaled down in size to become microPET, but due to fundamental physics limitations the resolution improvement is limited to about 1 mm (Levin and Hoffman 1999).

These imaging modalities do not fulfil all the requirements for small animal studies. In gene expression studies, it is desirable to use molecularly specific contrast agents to precisely localize patterns of expression. Of the medical imaging modalities, microPET is most suited for molecular specificity.

Optical imaging techniques are desirable due to the multitude of molecularly specific contrast agents that have been developed over many years of microscopy. However, attempts to move microscopic methods up to larger scales have met with limited success. Confocal microscopy is limited to a few hundred microns in penetration depth (Hecksher-Sørensen and Sharpe 2001), and even multiphoton microscopy is limited to less than a millimetre penetration (Potter *et al* 1996). Though both have extremely high resolution, they are also unsuited to the task of imaging whole organs or patterns of gene expression throughout an entire specimen without resorting to sectioning techniques. Alignment of serial section images is time-consuming, and the process of sectioning may obscure subtle morphological differences of interest when comparing mutant and wildtype (Hecksher-Sørensen and Sharpe 2001). These microscopic techniques also cannot accommodate absorbing molecular markers common in standard microscopy.

Other optical tomographic imaging methods such as optical diffusion tomography (ODT) (Arridge 1999) or optical coherence tomography (OCT) (Schmitt 1999) are also potentially suitable modalities for small animal imaging. ODT provides specimen coverage of several centimetres, but so far has only been able to obtain images with resolutions on the order of millimetres, insufficient to resolve patterns of gene expression. OCT is able to image at a resolution of a few microns at specimen depths of several millimetres. Recent advances in molecularly specific contrast agents show promise (Yang 2005), but do not provide the full range of molecular specificity obtained with common microscopic contrast agents.

As a result, there is a need for an imaging technique that has large specimen coverage, cellular-level resolution and molecular specificity. Over the past few years, several techniques have been presented to satisfy this need. Block-face or episcopic imaging (Weninger and Mohun 2002) embeds a sample, images its surface, removes the imaged layer and continues the process with the newly exposed tissue. However, the use of fluorescent markers commonly used in molecular imaging has not yet been reported. Selective plane illumination microscopy (Huisken *et al* 2004) illuminates a specimen with a sheet of excitation light and images the emitted fluorescence with an orthogonal camera-based detection system. It cannot accommodate absorbing molecular markers commonly used with brightfield microscopy.

Optical projection tomography (OPT) (Sharpe *et al* 2002) is a relatively new technology that obtains cellular level resolution, large specimen coverage (≈ 1 cubic centimetre), and is able to use both absorbing and fluorescent molecular markers. Use of the technology has begun to spread (von Both *et al* 2004, Lickert *et al* 2004, Kerwin *et al* 2004, Tucker *et al* 2004) and it is clear that it will become a widely used tool in the study of model organisms such as the mouse.

However, OPT images suffer from several artefacts which reduce their overall quality. There are several improvements that can be made to the technique to improve its accuracy and

extend its capabilities by correcting for these artefacts. Although the apparatus for OPT will undergo engineering redesign over time, the issues described in this paper are general to all OPT experiments and need to be addressed.

In this paper, we present methods for improving OPT by correcting imaging artefacts due to nonidealities in key components of the OPT technique. Reconstructed images demonstrate smear artefacts due to illumination intensity fluctuation, smear artefacts due to fluorescent signal decay, ring artefacts due to CCD pixel-to-pixel variability, and unique ‘detector edge’ artefacts caused by a non-zero background signal. Methods to correct these artefacts are presented. A reconstructed image with a poorly aligned centre of rotation results in distortions of the image, so we provide an automated method for centring based on the variance of the reconstructed images. Finally, reconstructions from truncated projections produce a bowl artefact. The method we propose to correct this artefact also allows higher resolution data to be obtained from a region of interest (ROI) without dissection of the specimen.

2. Description of optical projection tomography

Since optical projection tomography has been reviewed elsewhere (Sharpe 2004), only a brief description is provided. A small (≈ 1 cubic centimetre) transparent specimen is embedded in agarose, dehydrated, then immersed in a 1:2 mixture of benzyl alcohol and benzyl benzoate (BABB). This process replaces water (refractive index = 1.33) with BABB (refractive index = 1.56), which reduces scattering throughout the tissue (Müller *et al* 1993, Tuchin 2000, 2002). The use of a refractive index-matched liquid for imaging to reduce optical scattering (also known as ‘clearing’ or ‘clarifying’) has been previously used in standard microscopy (Klymkowsky and Hanken 1991), OCT (Vargas *et al* 1999) and confocal microscopy (Gard 1993, Zucker *et al* 1998). The use of BABB as a liquid that is index-matched to refractive indices of tissues (Bolin *et al* 1989) allows one to assume that scattering is minimized and that photons travel an approximately straight-line path through the specimen. Currently no attempt is made to correct for any residual scattering of light.

The refractive index-matched specimen is then placed in a BABB bath with flat parallel glass windows and an image of the specimen is formed using an optical microscope as shown in figure 1(a). OPT images can be created in two different modes: emission OPT (eOPT) and transmission OPT (tOPT). In the case of eOPT, fluorophores throughout the sample are excited by widefield illumination from a mercury vapour arc lamp. Photons emitted from the fluorophores are separated from the incident illumination by a chromatic filter, and are collected by the optical system to create an image. In the case of tOPT, diffuse white light is transmitted through the specimen and collimated by a lens to create an image. These two complimentary modes require different image reconstruction and suffer from different artefacts.

The image formed by the microscope is recorded by a cooled charge coupled device (CCD) camera, in order to minimize noise and increase detection efficiency. The data recorded by a pixel come from a narrow cone of light defined by the lens. This cone of light approximates a strip integral projection through the specimen. The axes of all the cones of light collected by the pixels in the CCD frame diverge by less than 0.3° , allowing the cones of light captured by the pixels in a CCD frame to be approximated as parallel ray projections through the sample. Each image recorded by the CCD is termed a view.

In all OPT views, there is a limited region in the object, defined by the depth of field, over which the specimen is in acceptable focus. Any part of the specimen not spanned by the depth of field is out of focus in the recorded view. In OPT, the depth of field is positioned such that it spans the region of the specimen located between the rotational axis and the part

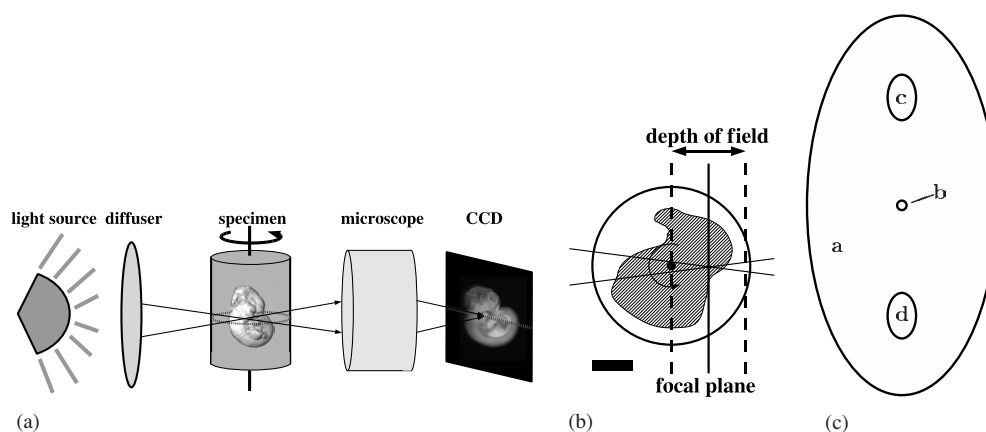


Figure 1. Diagram of optical projection tomography (OPT). (a) Diffuse light passing through the specimen is collimated by the microscope and recorded by a CCD. The specimen is rotated and views at multiple angles are acquired. (b) The depth of field is positioned over the half of the specimen nearest the detector. The scale bar represents 2 mm. (c) Simulations were performed with a phantom consisting of four ellipses (a)–(d), as shown here and as described in table 1.

of the specimen nearest the optical imaging components. Each OPT view thus superimposes in-focus data from the proximal half of the specimen, and out-of-focus data from the distal half of the specimen (figure 1(b)).

Views acquired in eOPT mode represent the integrated intensity of sources of fluorescent photons through the specimen along a given ray. In contrast, tOPT views represent the number of photons that were not attenuated while traversing the specimen. The tOPT views must be transformed according to Beer's law, standard in x-ray CT, in order to obtain sums of attenuation coefficients along the projection cones, necessitating sample removal and capture of brightfield images. Each view is divided by a low noise estimate of the illumination that is obtained by averaging several brightfield images.

The specimen is rotated stepwise through a complete revolution with views acquired at each step. A complete revolution is necessary in order to obtain in-focus data from all parts of the specimen. The CCD is oriented such that the rows of CCD pixels are aligned perpendicular to the rotational axis. The temporal sequence from a row of detectors forms a sinogram that reconstructs the corresponding slice using standard convolution filtered back-projection (Slaney and Kak 1988). The reconstruction of all slices yields a 3D volumetric representation of the specimen.

Throughout this paper, the term OPT will be used unless the distinction between eOPT and tOPT is relevant.

2.1. Noise characteristics

The average signal recorded by one pixel of the CCD in one view typically exceeds 3500 photons, as determined from a photon transfer curve (Janesick *et al* 1987). The Poisson noise on this average signal is less than 2%. Thus artefactual signals must be reduced to 1% to keep them below the level of the noise.

3. Methods

Parallel-ray projection simulations were used to evaluate and illustrate the artefacts caused by nonideal conditions. For the simulations, a digital test object designated a 'numerical phantom'

Table 1. Properties of the phantom used in parallel-ray projection simulations and shown in figure 1(c). All units are in mm unless otherwise noted. All elements have an index of refraction $n = 1.56$. For eOPT, the phantom elements have the property of concentration, and for tOPT, the phantom elements have the property of attenuation coefficient.

Element	Centre coordinates		Major axis	Minor axis	Rotation (°)	eOPT conc. (mm^{-1})	tOPT atten. coeff. (mm^{-1})
a	0.0,	0.0	2.0	1.0	90.0	1.00	1.00
b	0.0,	0.0	0.05	0.05	0.0	1.75	1.75
c	0.0,	0.58	0.24	0.15	90.0	6.75	6.75
d	0.0,	-0.58	0.24	0.15	90.0	6.75	6.75

is shown in figure 1(c) and table 1. It represents an axial section through a mouse embryo. For eOPT, the two ellipses of high intensity represent two very strong fluorescent signals, such as the blood-filled vasculature of an autofluorescent scan. For tOPT, these circles represent two highly attenuating objects, such as from India Ink contrast agent in the vasculature. The small circle at the centre of the phantom is included to demonstrate conspicuity of any small object within the embryo. Sinograms of the phantoms were generated using 1500 views over a complete revolution to obtain reconstructed images free from angular sampling effects that arise from the artificial sharp edges in the numerical phantoms that are less likely to be encountered in biological specimens.

Actual OPT data from three E12.5 mouse embryos were acquired on an OPT device that included a Leica MZFLIII stereomicroscope using a Plan 0.5 \times , 135 mm working distance objective lens (Leica 10446157), and a 1.0 \times camera lens with an 80 mm tube length (Leica 1445930). The images were recorded by a 1376 \times 1036 pixel (6.45 μm pitch size, binned 2 \times 2) Retiga Exi CCD that was thermoelectrically cooled to -40°C . Specimens imaged with eOPT were illuminated by a 100 W mercury vapour lamp (Leica 10504069) attached to the microscope housing, while specimens imaged for tOPT were illuminated by a light diffuser that consisted of a halogen lamp and two sheets of white plastic separated by 1 cm. The rotational step size was 0.9° , with a total of 400 images acquired in a complete revolution. Typical exposure times ranged from 50 ms to 3000 ms, and total imaging time ranged from 180 s to 12 000 s.

4. Key components of OPT and correction of associated artefacts

4.1. Illumination

Each view acquired in an OPT data set collects a 2D array of parallel-ray projections through the specimen. The entire specimen must be wholly and uniformly illuminated thus requiring widefield illumination. Since the OPT signal is proportional to the intensity of the incident illumination, it is necessary to have light sources that are stable over the course of an imaging session.

4.1.1. Emission OPT. The most common source of widefield fluorescent illumination is the mercury arc gas discharge lamp. These lamps generate light of all wavelengths, which allows the use of the full range of optical fluorophores. Unfortunately, arc lamps suffer from both short- and long-term instability which worsen with the age of the lamp. This fluctuation can range from 1 to 4% in a new lamp, and up to 10% as the lamp ages. Even power stabilized mercury lamps are subject to short-term fluctuations of approximately 1% (Woodlee *et al*

1989). Since the fluorescent output is proportional to the intensity of incident light, eOPT views are subject to the same fluctuations.

We inserted a power detector into the OPT housing after the excitation light filter to monitor the intensity of incident mercury lamp light. The power meter was positioned to collect incident light that was scattered from the OPT apparatus housing and no object was introduced into the light path. The average fluorescent signal in each view obtained from the CCD shows fluctuations over time similar to that measured by the incident light meter (figure 2(a)). The average pixel intensities were first corrected for signal decay from photobleaching as described in section 4.2. The distribution of residual fluctuations approximated by a Gaussian distribution with a standard deviation of about 1.2%. The correlation coefficient of the decay-corrected average intensities and the fluctuations of the mercury lamp was found to be 0.78 with a p -value <0.0001 . The inexact correlation is due to fluorescent decay times of fluorophores and limited data sampling rate of the power meter.

A simulation was used to determine the effect of incident light fluctuations. Each view in the sinogram of the phantom was multiplied by the signal modulation recorded by the incident light meter to simulate the temporal intensity fluctuations. Comparison of the reconstruction without signal fluctuation (figure 2(b)) to the reconstruction with simulated signal fluctuation (figure 2(c)) demonstrates bright and dark smears originating from high-intensity objects. A second simulation using intensity fluctuations from a Gaussian distribution with standard deviation of 5% was performed to examine the artefacts potentially caused by an older mercury lamp (figure 2(d)). The smear artefacts evident in the reconstructions are more severe than those in the previous reconstruction.

A correction factor to compensate for signal fluctuation was determined by subjecting the average fluorescent signal over all views to a low-pass filter in order to obtain much smoother and gradual fluctuations, then normalizing the views to match the filtered curve. The corrected reconstructed image for the views that were subject to the 5% fluctuation is shown in figure 2(e). The smearing artefact is no longer visually appreciable. Plots of a section of the central column located between the lower large circle and the middle small circle of the phantom are shown in figure 2(f) to demonstrate the differences.

The reconstructed image values through a region of constant intensity typically vary due to the limited number of views and the weighting filter used in the filtered backprojection process. The random intensity fluctuations at different view angles increase these variations and introduce location-dependent differences from the expected reconstruction values, as shown in figure 2(f). Some image values are higher than expected, as shown in the 2.5% simulation between -0.42 and -0.38 mm (figure 2(f)), while other image values are lower than expected, as shown in the 2.5% simulation between -0.3 to -0.17 mm. The 5% simulation exhibits similar location-dependent variations that are most evident at -0.35 mm, where the reconstruction values are higher than expected, and at -0.25 mm, where the values are closer to expected. The variations have been reduced in the corrected 5% simulation, and the streak artefacts are no longer evident (figure 2(e)).

Although this method retains the low-frequency fluctuations of the lamp (standard deviation of 0.5%), it removes the more significant high-frequency fluctuations that are the primary cause of the smearing artefact. This computational method also has the advantage that it does not require a power meter to be inserted into the OPT housing.

4.1.2. Transmission OPT. In tOPT, white light from a halogen lamp is passed through a diffuser onto the specimen, and is subsequently collimated by the optical system of the microscope. We have used a power detector and meter to measure the output intensity of

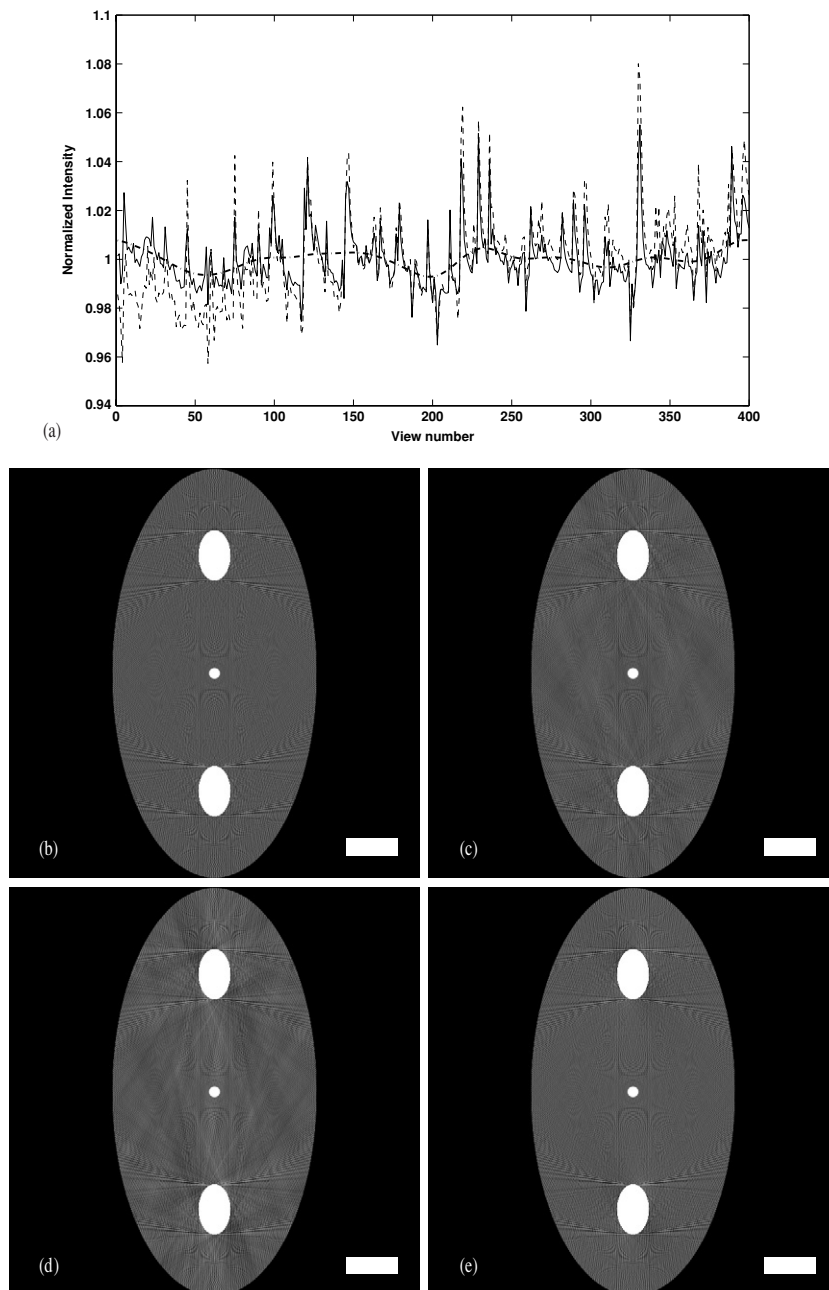


Figure 2. (a) Power fluctuations in the mercury lamp (---) are evident in the total fluorescent intensity of the views (—). Passing the fluctuations through a lowpass filter removes the high-frequency fluctuations (— · —). The reconstruction without signal fluctuation (b) is provided for comparison to reconstructions with (c) the recorded intensity fluctuations and (d) simulated intensity fluctuations of standard deviation 5%. (e) The corrected reconstruction does not exhibit the smear artefacts. The scale bars represent 0.25 mm. (f) Plots of a section of the central column, located between the lower large circle and the middle small circle of the phantom, show the differences between the cases of no fluctuation, fluctuation and corrected fluctuation.

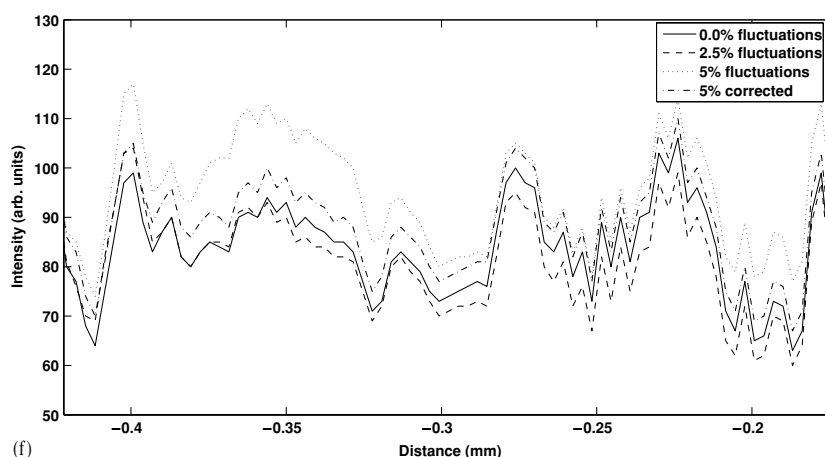


Figure 2. (Continued.)

the halogen lamp and have determined that the lamp is stable to better than 0.2%. This is satisfactory stability and no compensation needs to be introduced.

4.1.3. Comparison to x-ray CT. X-ray tubes common in x-ray CT generally require a warm-up period, during which time the x-ray output fluctuates significantly. After the tube has stabilized, the output flux stability is typically better than 1%. The level of fluctuation does not cause streaking artefacts as described above.

4.2. Signal decay

4.2.1. Emission OPT. Most fluorophores used in optical imaging are subject to photobleaching (Pawley 1995), resulting in an exponential decay of fluorescent signal with respect to exposure time. An eOPT view of a non-rotating E12.5 mouse embryo was acquired 400 times to determine the signal loss over the typical OPT imaging period. The overall signal loss from the specimen was approximately 8% from the first to last view. Other data from rotated eOPT data sets of E9.5 to E12.5 mouse embryos demonstrated a signal loss between 2–25% over the total imaging time. An exponential curve was fitted to the sum of pixel intensities versus image number, shown in figure 3(a), to verify that the signal loss followed an exponential decay to first order.

Simulations of exponential signal decay were performed using the numerical phantom. Total signal loss in the simulations ranged from 2% to 25% (3(c), (d)) and is compared to a reconstruction without signal decay (figure 3(b)). Exponential signal decay results in both a bright and dark streaking artefact originating from high intensity objects that are oriented along the ray paths of the first and last view of the object.

The cause of this artefact originates in the filtered backprojection reconstruction algorithm. The initial views are of a higher intensity than the mean view, and as a result the filter generates projections with greater peaks and negative lobes compared to the mean intensity of all projections. Similarly, the last view generates smaller peaks and negative lobes than the mean and does not adequately compensate for the more intense views.

The effects of signal decay can be compensated by normalizing each eOPT view according to the rate of signal decay, which can be determined by fitting an exponential curve to average

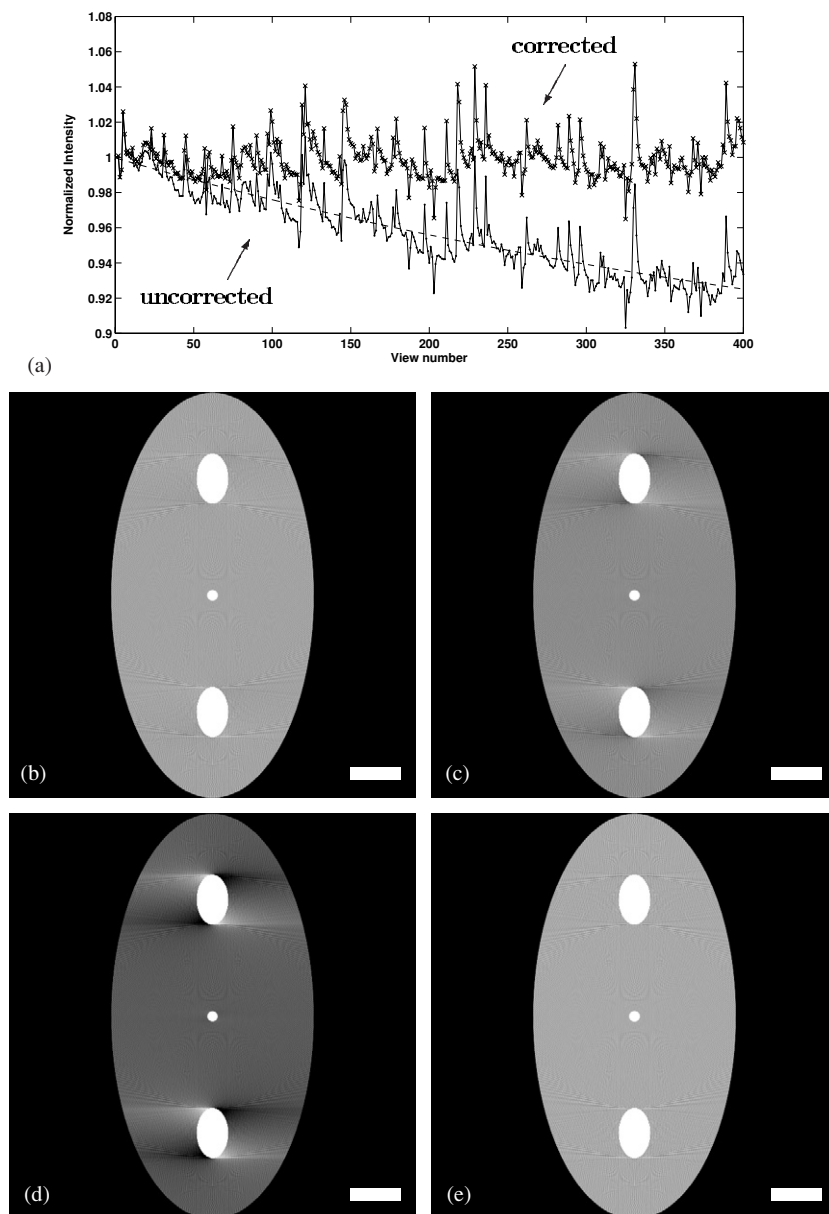


Figure 3. The signal decay due to photobleaching in eOPT (●) can be corrected by normalizing according to an exponential fit (---). The corrected view intensities (×) demonstrate no decay. The reconstruction without signal decay (b) is used for comparison to reconstructions of sinograms with a 2% signal decay (c) and a 25% signal decay (d). The result of signal decay is an artefact of bright and dark streaks originating from high intensity objects. (e) Correcting the signal decay of (d) results in no visible artefact. The scale bars represent 0.25 mm.

fluorescent intensities in each view as in figure 3(a). Each eOPT view is then multiplied by the appropriate normalization constant to correct for signal decay, and reconstruction

proceeds normally. The resulting reconstruction demonstrates negligible signal decay artefact (figure 3(e)).

4.2.2. Transmission OPT. Photobleaching of photon attenuating molecules is also possible; however, we observed no tOPT signal decay with respect to time to within 0.1%.

4.2.3. Comparison to x-ray CT. No bleaching loss of signal occurs in x-ray CT.

4.3. Detection

It is well known that the average of a CCD response to photon intensity is not perfectly linear over the full dynamic range of the CCD. In addition, the response of each pixel varies slightly from the average. This effect arises from fixed pattern noise, dark current, read noise and variation in pixel sensitivity (Pawley 1995). Most CCDs also contain ‘bad’ pixels whose response varies greatly from the other pixels on the chip. The intensities recorded by these pixels are generally considered unreliable and unusable. Finally, dust and other foreign objects within the optical system can create inaccurate readings on the CCD on the order of $\sim 1\%$. Calibration of the CCD is generally required prior to mathematical manipulation of the images.

We calibrated the photon response of the CCD (Pawley 1995) in order to determine the extent of the imperfections. A diffuse white light was created by shining a halogen lamp onto a diffuser, through the microscope and onto the CCD. The microscope was defocused by placing the focal plane more than 5 cm from any object, in order to obtain a uniform intensity across the CCD. A series of images with increasing exposure time from 0 ms to 25 ms was acquired for calibration. The photon flux was assumed to be proportional to exposure time. Several images were collected at each exposure time and averaged to minimize photon noise. A series of images with the shutter closed was acquired and averaged at each exposure time, then subtracted from the averaged bright images, to remove the effect of the CCD dark current. The intensities of each pixel versus the exposure times were fitted to a second order polynomial to determine a calibration curve for several pixels. Two calibration curves from two different pixels demonstrate a very similar trend figure 4(a), but the differences are obvious when comparing the residuals from a linear fit of the mean image intensity (figure 4(b)). The polynomial fit agreed with the measurements to within 1%.

The distribution of the pixel responses to a given exposure time followed an approximately Gaussian distribution with a standard deviation which was 0.3% of the mean. Four pixels over the entire CCD deviated by more than 7σ from the mean, and these were labelled as ‘bad’ pixels. Two ‘bad’ pixels were found on a single row of the CCD.

4.3.1. Emission OPT. The observed CCD nonlinearities were simulated with the digital phantom to determine their impact on the reconstructed image. The effects of a general nonlinearity versus a pixel-by-pixel variation in photon response were considered separately. A nonlinearity was applied to the pixel readouts of the projections, using the polynomial coefficients of an arbitrary pixel that were determined in the previous step. The effect of variable CCD pixel sensitivity in eOPT was simulated by multiplying each pixel in all views by a random number from a Gaussian distribution centred about 100% with a standard deviation of 0.3%. Two ‘bad’ pixels to represent the two bad pixels on the same slice were simulated by multiplying two pixels in all views by 120% and 80%.

A streak artefact is evident in eOPT images reconstructed from projections that were subject to the nonlinearity. The streak artefact evident in figure 4(c) is of negative intensity,

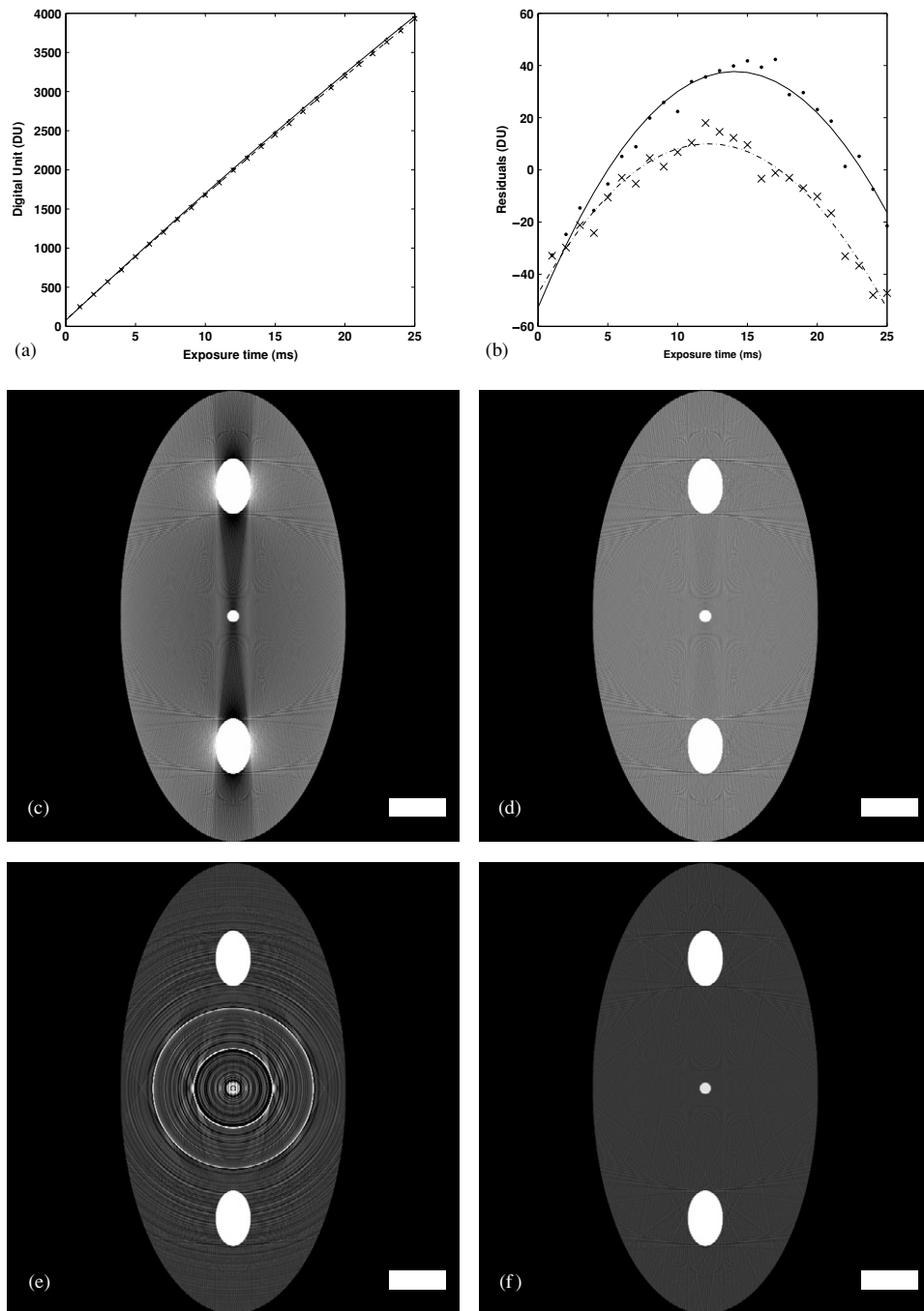


Figure 4. Calibration curves for two different pixels follow the same general shape (a) but the residuals from a linear fit to the CCD mean at each exposure (b) clearly demonstrate the different responses. Streak artefacts arise in eOPT reconstructions if the CCD is not calibrated (c) but can be avoided with proper calibration (d). Variation in pixel response and 'bad' pixels lead to ring artefacts in eOPT (e), but can be similarly avoided (f). tOPT reconstructions without CCD calibration results in similar artefacts (g), which can also be avoided by proper CCD calibration (h). The scale bars represent 0.25 mm.

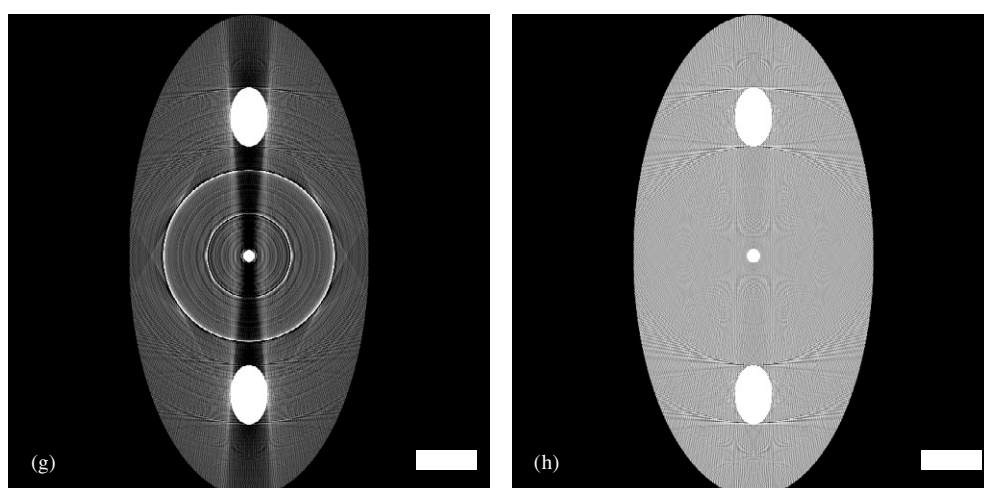


Figure 4. (Continued.)

originates from objects of high intensity, is most conspicuous in homogeneous regions, and is present along the angles at which the objects of high intensity are aligned. Note that the streak could also have positive intensity depending on the nonlinear response of the CCD. Calibration of the CCD using the polynomial prevents the streak artefact (figure 4(d)).

eOPT images reconstructed from projections subject to pixel-to-pixel variation in sensitivity demonstrate a ring artefact, as shown in figure 4(e), which is characterized by concentric rings about the rotational axis. The artefact caused by a 'bad' pixel consists of a single bright ring at a radius equal to the distance of the 'bad' pixel from the location of the rotational axis on the CCD.

The concentric ring artefact caused by pixel-to-pixel variations can be reduced by compensating for the photon response of each individual pixel. The artefact created by the 'bad' pixel can be corrected by replacing the recorded intensities by the mean of its eight neighbours in all views, prior to reconstruction. The result of this final implementation does not exhibit the ring artefact (figure 4(f)).

4.3.2. Transmission OPT. Simulations for tOPT modelled both photon response nonuniformity and variable pixel sensitivity simultaneously. The pixel-by-pixel nonlinear response was calculated using polynomial coefficients of several pixels that were previously calculated during CCD calibration.

While the artefacts generated by these imperfections (figure 4(g)) are similar to eOPT, the streak artefact in tOPT is due to the dark current of the CCD. A projection with photons that are completely attenuated registers a non-zero value and thus the log transform is calculated with an incorrect sum of attenuation coefficients. This effect is most significant for high attenuation ray paths but is present in all projections, with the severity proportional to the attenuation. The effect of nonlinearity is less significant in tOPT than eOPT due to the compression of contrasts created by the log transform of the projections.

The concentric ring artefact caused by variable pixel sensitivity is similar in tOPT as in eOPT, as shown in figure 4(g). The 'bad' pixel causes a single bright ring to appear. Proper calibration of the CCD prior to reconstruction corrects both the nonlinear and concentric ring artefacts (figure 4(h)).

Although modern CCDs have excellent linearity over a large response range, it should not be assumed that the linearity is adequate for computational imaging. Calibration of the CCD should be performed for both eOPT and tOPT to avoid the detection artefacts described.

4.3.3. Comparison to x-ray CT. The pixel-to-pixel variations contribute to the well-known ring artefact in x-ray CT (Tofts and Gore 1980), as they do in OPT. Nonlinearities of the detector response are often more pronounced due to greater nonlinearities in the scintillation detectors common in x-ray CT (Jorgensen *et al* 1998). In addition, pixel-by-pixel variations in detector response result in more significant ring artefacts, as contrast differences in x-ray CT images are often 1% or less. Similar calibrations of the detector and corrections of the measured signal to compensate for these variations are commonly employed to lessen or remove the ring artefact.

4.4. Background signal

4.4.1. Emission OPT. Ideally, background intensities in eOPT views would be zero, as there should be no sources of fluorescent photons in the media surrounding the specimen. In practice, background intensities are often several per cent of the mean signal. Using these projection values in a standard filtered-backprojection algorithm results in a reconstructed image that exhibits a 'bowl' artefact, shown in figure 5(a), similar to the x-ray CT bowl artefact created due to projection truncation. A plot through the central row of the image in figure 5(a) is shown in figure 5(b) to clearly demonstrate the 'bowl'. Two superimposed bowl artefacts are present if the rotational axis is not coincident with the centre of the detector. We have termed this the 'detector edge' artefact. This bowl artefact arises due to the reconstruction algorithm's incorrect assumption of zero signal outside the field of view (FOV) (Gore and Leeman 1980).

To determine the cause of the non-zero background signal, a series of images with different configurations of the apparatus was acquired. The configurations were: (A) standard configuration of agarose, specimen, BABB, and cuvette within the apparatus, (B) agarose but no specimen, (C) cuvette and BABB only, (D) and empty cuvette, and (E) nothing. The images were compared by taking their ratios, and were also visually inspected. The images of cuvette and BABB (C) were found to closely and consistently approximate the background signal of an eOPT view.

Subtracting the image in (C) from all eOPT views reduces the background intensity values close to zero. This method is superior to subtracting a constant background value from all views as any structure in the background signal is taken into account. Images reconstructed from eOPT views processed in this manner demonstrate a significantly reduced detector edge artefact, shown in figure 5(c).

4.4.2. Transmission OPT. In tOPT, the specimen is removed from the FOV and a brightfield image is captured. The agarose plug surrounding the specimen is larger than the FOV and thus all rays in the tOPT view suffer some attenuation that is not present in the brightfield image. However, attenuation caused by the agarose is <1% of the attenuation caused by the specimen and so does not result in any appreciable artefact.

4.4.3. Comparison to x-ray CT. X-ray CT, as a transmission tomographic imaging method, has similar properties to tOPT with respect to the background signal. In clinical x-ray CT, x-rays passing through the air surrounding the patient are not attenuated. X-ray μ CT specimens are often embedded in a wax or plastic medium, and the entire mount is included in the FOV.

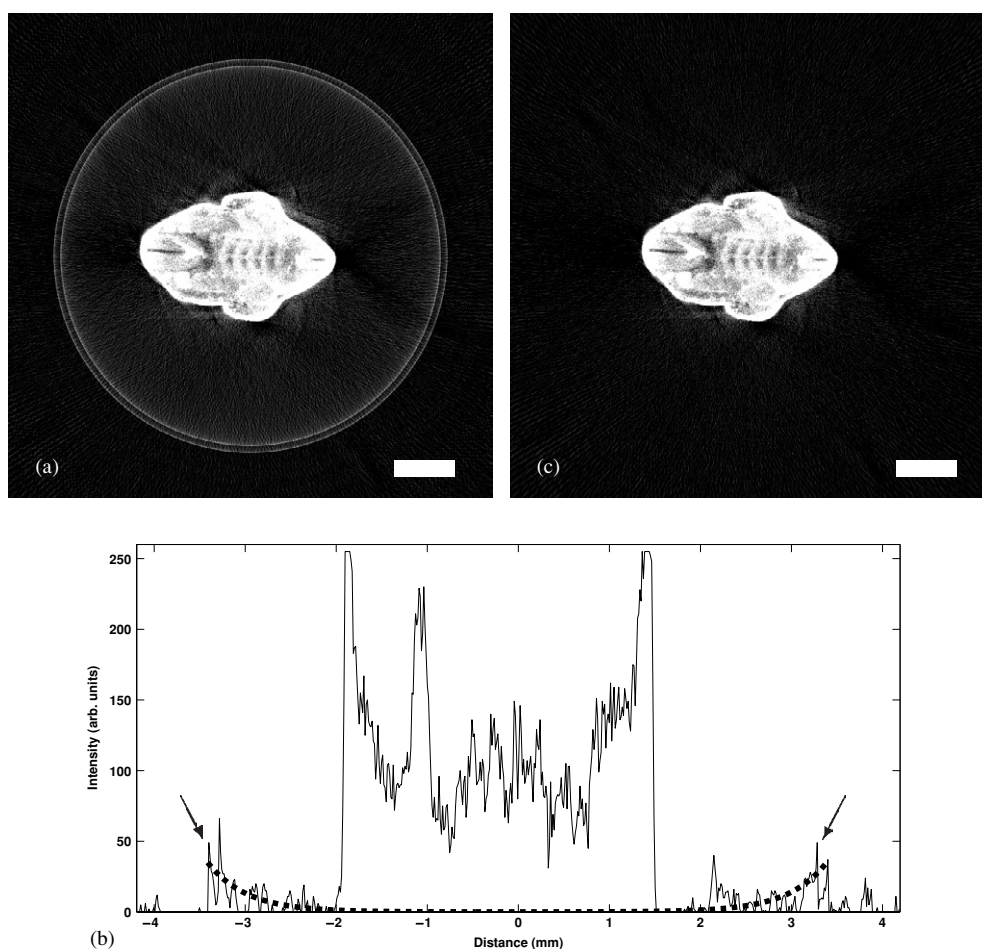


Figure 5. (a) Two bright concentric rings in the reconstruction plane, called the detector edge artefact, are evident in these eOPT reconstructions of the lower body of an E12.5 mouse embryo. (b) A plot through the central row of (a) demonstrates the 'bowl' artefact (arrows and (---)). (c) Subtracting an eOPT background image eliminates the artefact. The scale bars represent 1 mm.

Outside the mount region, x-rays pass without attenuation. As a result, there is no residual background signal.

4.5. Determination of centre of rotation for reconstruction

4.5.1. Emission and transmission OPT. Images reconstructed from sinograms with incorrectly identified centres of rotation exhibit mild to severe artefacts depending on the offset error. A severe (10 pixel) and slight (1 pixel) error is shown in figures 6(a) and (b). If the position of the rotational axis is not well known prior to data acquisition, it must be determined post-acquisition in order to minimize this artefact. The rule of thumb in x-ray CT is to identify the location to within a quarter of a detector pixel.

One method to accurately place the rotational axis in the sinogram is to reconstruct the same sinogram many times, each with a differently identified centre of rotation. A user can then step through each image, choose the image which is visually superior and use that centre

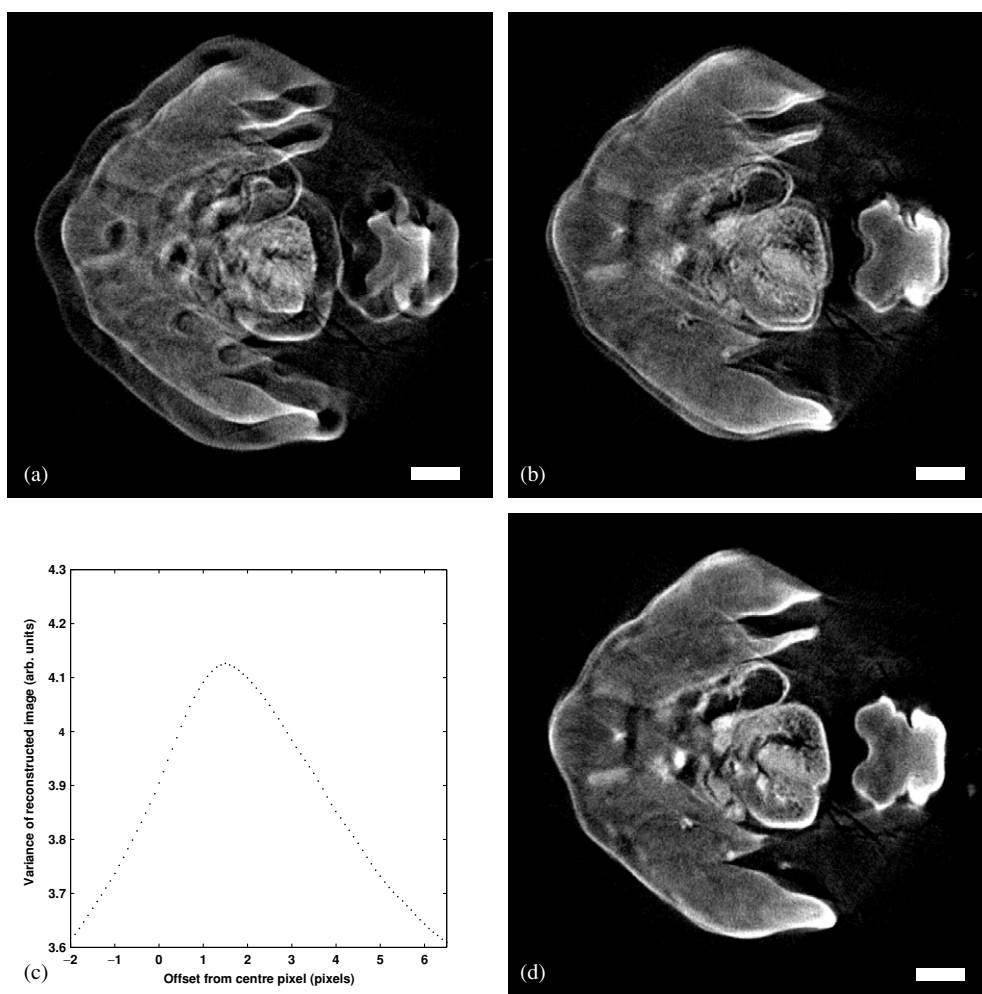


Figure 6. Severe (a) or slight (b) artefacts arise from an incorrectly identified rotational axis position, as demonstrated in these reconstructions of the cardiac region of an E12.5 mouse embryo. The variance of a series of test reconstructions (c) is a maximum at the true position of the rotational axis. The reconstruction with the correctly identified rotational axis position is shown in (d). The scale bars represent 0.5 mm.

of rotation for reconstruction all slices. This is time consuming, and in practice it is difficult to distinguish between subpixel differences in alignment.

The reconstruction of a sinogram with a misaligned rotational axis can be considered to be a convolution of the correctly reconstructed image and a blurring function. The position of the rotational axis can then be determined by reconstructing a series of images with differently assumed positions of the rotational axis, and calculating the variance of each reconstruction. The reconstructed image that has the maximum variance is closest to the ideal reconstruction, as it is the least blurred. A similar ‘autofocus’ algorithm using the variance of the image has been previously used in standard microscopy (Groen *et al* 1995). We implemented this method and found it to be effective for identifying the centre of rotation to an accuracy better than 1/8th of a pixel. The variance curve in figure 6(c) demonstrates a very smooth approach

to the true location of the rotational axis. A reconstruction with the correct location of the rotational axis is shown in figure 6(d). Correction for the detector edge artefact must precede this step as that artefact's presence can lead to erroneous results.

4.5.2. Comparison to x-ray CT. X-ray cone beam CT commonly uses a cross-correlation between opposing views in order to determine the location of the rotational axis. The effectiveness of this process is limited in OPT, as opposing views differ due to the effects of the depth of field. Objects in focus in one view are out of focus 180° later, and vice versa. Thus the usual methods of x-ray CT are not applicable.

4.6. Projection truncation

4.6.1. Emission and transmission OPT. Often the structure of interest (or region of interest, ROI) is only a subregion within the specimen rather than the entire specimen, for example the heart within a mouse. It would be advantageous to obtain better resolution over the ROI by maximizing the number of detectors that span it. This can be done by positioning the ROI to fill the FOV over all views. The parts of the specimen that are outside the ROI are not captured and truncated projections are recorded. Reconstruction of a sinogram with truncated projections (figure 7(a)) results in a bowl shaped artefact over the reconstructed image which is most noticeable at the boundaries of the reconstruction region as shown in figure 7(b). These are similar to but more severe than the bowl artefact resulting from non-zero background signal described in section 4.4.

The variable magnification of OPT allows one to address this situation with a very good estimate of the missing data. High resolution OPT views of the ROI can be obtained, and the incomplete projections can be extrapolated with data from lower resolution views of the same specimen obtained in a subsequent scan. As a result, the specimen need not be dissected, the complete ROI is imaged at its highest resolution, the missing data are well estimated, and the gross positioning and relative size of the ROI within the whole specimen is maintained.

We tested this method on the liver in an E12.5 mouse embryo. The specimen was positioned such that the liver was centred in the FOV at a total magnification of 3.15×, and an eOPT scan was recorded. The depth of field was positioned at the higher magnification in order to ensure that the ROI was in-focus over the high-resolution scan, similar to figure 1(a). The magnification of the microscope was then reduced to 1.25×, and an eOPT scan of the complete specimen was recorded. The stereozoom microscope is parfocal between zoom settings, and so the position of the focal plane is retained. The depth of field increases at the lower zoom setting, encompassing more of the specimen. Although the depth of field does not encompass the full front-half of the specimen as is typical in OPT, the part of the specimen that ends up out of the depth of field, is near the edge of the specimen and some blurring to this region is tolerable.

The lower resolution views (figure 7(c)) were linearly interpolated to match the detector spacing of the higher magnification views (figure 7(d)), and a cross-correlation algorithm was performed for 20 views spread at 18° around the revolution to align the high-resolution views within the low-resolution view. The pixel shifts from the cross-correlation data were averaged to obtain a single shift value for all views. The lower resolution data were shifted by linear interpolation to correct for subpixel alignment.

The high resolution views were not simply high resolution copies of the lower resolution views. Increasing the magnification also increases the collecting and resolving power, or the numerical aperture (NA), of the optical system, while decreasing the depth of field. Some objects that were in focus in the low resolution view are out of focus in the high resolution view.

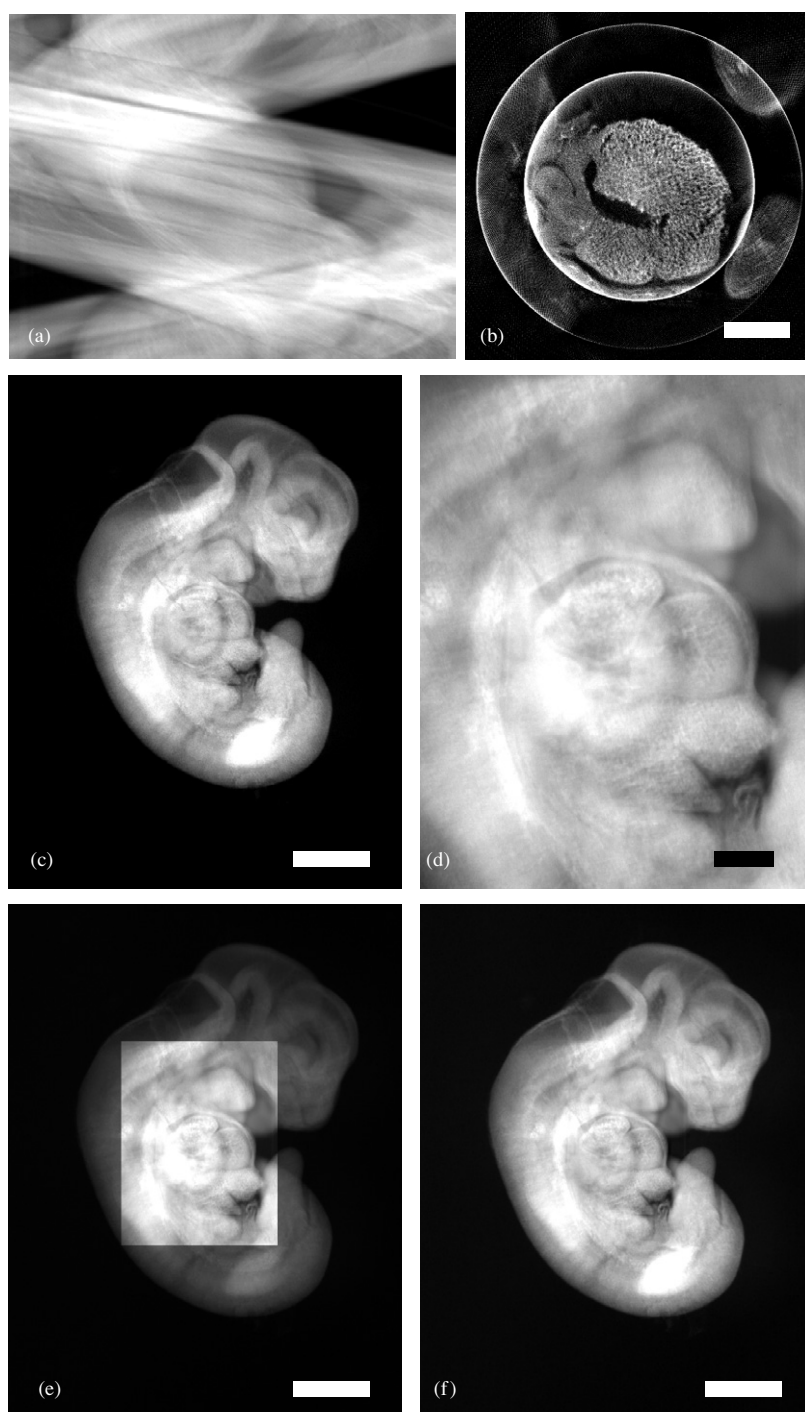


Figure 7. A sinogram with truncated projections (a) leads to a 'bowl' artefact over the reconstructed image of the liver of an E12.5 mouse embryo (b). A low-resolution view (c) and high-resolution view (d) are combined (e) to obtain a good estimate of the data outside the field of view in the high resolution image. (f) Intensity scaling the low-resolution view before combining the views results in a better estimate. The scale bars represent (b) 0.5 mm, ((c), (e), (f)) 1 mm and (d) 0.3 mm.

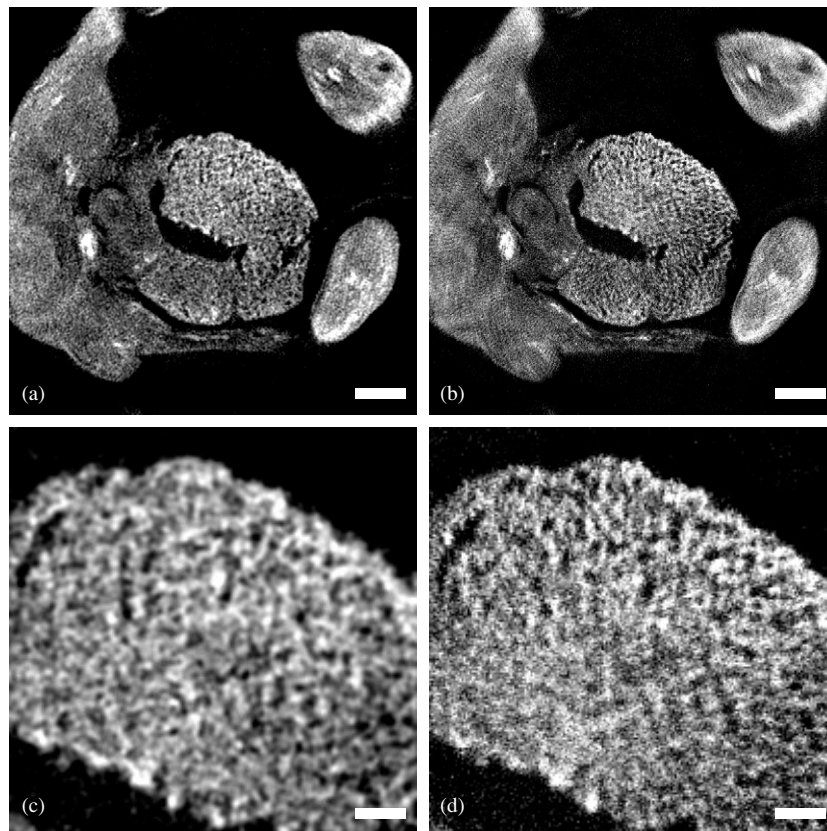


Figure 8. A reconstruction of the low-resolution projections (a) has complete specimen coverage but shows less detail than the reconstruction of high resolution projections using data from the low resolution projections to estimate the missing data. (b) The bowl artefact in figure 7(b) is no longer visible with the new method (c). Details of the low resolution reconstruction (c) show significantly less detail than the high-resolution reconstruction (d). The scale bars represent ((a), (b)) 0.3 mm and ((c), (d)) 0.1 mm.

The larger acceptance cone also collects more light, and high resolution views acquired with the same exposure time are generally brighter. Scaling exposure times to obtain data sets with similar mean signal values still result in regional differences in image intensity (figure 7(e)). Normalization is required to properly fit the high-resolution data into the interpolated low-resolution data.

Both the high-resolution view and the interpolated low-resolution subregion were passed through a Gaussian low-pass filter in order to obtain corresponding images with approximately the same frequency content. The two images were divided to obtain scaling factors for the high-resolution image to fit smoothly within the interpolated low-resolution image while preserving the high-frequency information. The final view incorporating both low- and high-resolution data demonstrates no intensity discontinuities at the borders of the high resolution view (figure 7(f)).

The results of reconstructions are shown in figures 8(a)–(d). The reconstruction in (b) is visually superior to the reconstructions in (a) as the higher resolution reconstruction contains more detail in the ROI. Details of (a) and (b) are shown in figures 8(c) and (d). The reconstruction in 8(b) does not demonstrate any noticeable bowl artefact as in figure 7(b).

4.6.2. *Comparison to x-ray CT.* There are several algorithms to account for projection truncation in x-ray CT, all of which involve estimating the missing data using the other elements in the detector array of the same view as a guide (Ohnesorge *et al* 2000, Lewitt 1979). The estimation assumes that the intensities form a generally smooth function which tails off to zero. However, these methods do not preserve the structure of data outside the FOV and in many cases still create imaging artefacts. Merging zoomed data as presented here is not possible in cone or fan beam x-ray CT because of the change of divergent beam angles between the zoom levels.

5. Conclusion

We have identified non-ideal performance problems with the OPT methodology, described the artefacts they create, and presented solutions for each of the following problems:

- Fluctuations in incident illumination cause a smear artefact that can be removed by normalizing OPT views to remove high-frequency temporal fluctuations in total view intensity.
- The eOPT signal decays with respect to time due to photobleaching effects. This can be corrected by normalizing each view according to the signal decay rate.
- Nonlinearity and dark current in the CCD photon response generates streak artefacts in both eOPT and tOPT that can be corrected by proper calibration of the CCD. Pixel variability in the CCD camera causes a ring artefact that can be removed or lessened by correcting the measured signal to actual signal prior to reconstruction. A 'bad' pixel causes a single ring in the reconstructed image, which can be corrected by replacing the value of the 'bad' pixel by the mean of the neighbours prior to reconstruction.
- The background signal of an eOPT view is non-zero, which leads to a 'bowl' artefact, termed the 'detector edge' artefact. This can be removed by subtracting a background image from each view.
- Projection alignment can be automatically determined by calculating the variance of a series of reconstructions with differing locations of the centre of rotation. The reconstructed image with the largest variance is the closest to the true position of the rotational axis.
- Projection truncation creates a bowl-shaped artefact over the reconstructed image. Intensity scaled low resolution views can be used to estimate the missing data from truncated high resolution views. The result is a high resolution scan of a region of interest without dissecting it from the specimen and with negligible truncation artefacts.

Correction of all of these artefacts improves OPT image quality and accuracy using easy to implement solutions to reduce or remove the impact of nonidealities in the imaging system.

Acknowledgments

The research in this paper has been funded by the Canadian Foundation for Innovation and the Ontario Research and Development Challenge Fund. We would like to thank the British Medical Research Council for providing us with an OPT device. We also thank the Benoit G Bruneau lab for providing specimens for study. RMH holds a Canada Research Chair in Imaging, and JRW is funded with an Ontario Graduate Scholarship in Science and Technology.

References

- Arridge S R 1999 Optical tomography in medical imaging *Inverse Problems* **15** R41–R93
- Bolin F P, Preuss L E, Taylor R C and Ference R J 1989 Refractive index of some mammalian tissues using a fiber optic cladding method *Appl. Opt.* **28** 2297–303
- Flannery B P, Deckman H W, Roberge W G and D'Amico K L 1987 Three-dimensional x-ray microtomography *Science* **237** 1439–44
- Foster F S, Pavlin C J, Harasiwicz K A and Christopher D A 2000 Advances in ultrasound biomicroscopy *J. Ultrasound. Med. Biol.* **26** 1–27
- Gard D L 1993 Confocal immunofluorescence microscopy of microtubules in amphibian oocytes and eggs *Methods Cell Biol.* **38** 241–64
- Gore J C and Leeman S 1980 The reconstruction of objects from incomplete projections *Phys. Med. Biol.* **25** 129–36
- Groen F C A, Young I T and Ligthart G 1995 A comparison of difference focus functions for use in autofocus algorithms *Cytometry* **6** 81–91
- Hecksher-Sørensen J and Sharpe J 2001 3D confocal reconstruction of gene expression in mouse *Mech. Dev.* **100** 59–63
- Huisken J, Swoger J, Del Bene F, Wittbrodt J and Stelzer E H K 2004 Optical sectioning deep inside live embryos by selective plane illumination microscope *Science* **305** 1007–9
- Janesick J R, Klaasen K P and Elliott T 1987 Charge-coupled-device charge-collection efficiency and the photon-transfer technique *Opt. Eng.* **26** 972–80
- Johnson G A, Cofer G P, Gewalt S L and Hedlund L W 2002 Morphologic phenotyping with MR microscopy: the visible mouse *Radiology* **222** 789–93
- Jorgensen S M, Demirkaya O and Ritman E L 1998 Three-dimensional imaging of vasculature and parenchyma in intact rodent organs with x-ray micro-CT *Am. J. Phys.* **275** H1103–14
- Kerwin J *et al* 2004 3-dimensional modelling of early human brain development using optical projection tomography *BMC Neuro.* **5** 27
- Klymkowsky M W and Hanken J 1991 Whole-mount staining of *Xenopus* and other vertebrates *Methods Cell Biol.* **36** 419–41
- Levin C S and Hoffman E J 1999 Calculation of positron range and its effect on the fundamental limit of positron emission tomography system spatial resolution *Phys. Med. Biol.* **44** 781–99
- Lewitt R M 1979 Processing of incomplete measurement data in computed tomography *Med. Phys.* **6** 412–7
- Lickert H, Takeuchi J K, von Both I, Walls J R, McAuliffe F, Adamson S L, Henkelman R M, Wrana J L, Rossant J and Bruneau B G 2004 Baf60c is essential for function of BAF chromatin remodelling complexes in heart development *Nature* **431** 107–12
- Müller G, Chance B, Alfano R, Arridge S, Beuthan J, Gratton E, Kaschke M, Masters B, Svanberg S and van der Zee P (ed) 1993 *Medical Optical Tomography: Functional Imaging and Monitoring vol IS11* (Bellingham, WA: SPIE Press)
- Ohnesorge B, Flohr T, Schwarz K, Heiken J P and Bae K T 2000 Efficient correction for CT image artifacts caused by objects extending outside the scan field of view *Med. Phys.* **27** 39–46
- Pawley J (ed) 1995 *Handbook of Biological Confocal Microscopy* 2nd edn (New York: Plenum)
- Potter S M, Fraser S E and Pine J 1996 The greatly reduced photodamage of 2-photon microscopy enables extended 3-dimensional time lapse imaging of living neurons *Scanning* **18** 147
- Schmitt J M 1999 Optical coherence tomography (OCT): a review *IEEE J. Sel. Top. Quant. Electron.* **5** 1205–15
- Sharpe J 2004 Optical projection tomography *Annu. Rev. Biomed. Eng.* **6** 209–24
- Sharpe J, Ahlgren U, Perry P, Hill B, Ross A, Hecksher-Sørensen J, Baldock R and Davidson D 2002 Optical projection tomography as a tool for 3D microscopy and gene expression studies *Science* **296** 541–5
- Slaney M and Kak A C 1988 *Principles of Computerized Tomographic Imaging* (New York: IEEE)
- Tofts P S and Gore J C 1980 Some sources of artefact in computed tomography *Phys. Med. Biol.* **25** 117–27
- Tuchin V V 2000 Tissue optics: light scattering methods and instruments for medical diagnosis *SPIE Tutorial Texts in Optical Eng.* **TT38**
- Tuchin V V (ed) 2002 *Handbook of Optical Biomedical Optics* (Bellingham, WA: SPIE Press)
- Tucker A S, Watson R P, Lettice L A, Yamada G and Hill R E 2004 Bapx1 regulates patterning in the middle ear: altered regulatory role in the transition from the proximal jaw during vertebrate evolution *Development* **131** 1235–45
- Vargas G, Chan E K, Barton J K, Rylander H G and Welch A J 1999 Use of an agent to reduce scattering in skin *Lasers Surg. Med.* **24** 133–41
- von Both I, Silvestri C, Erdemir T, Lickert H, Walls J R, Henkelman R M, Rossant J, Harvey R P, Attisano L and Wrana J L 2004 Foxh1 is essential for development of the anterior heart field *Dev. Cell* **7** 331–45

- Weninger W J and Mohun T 2002 Phenotyping transgenic embryos: a rapid 3-d screening method based on episcopic fluorescence image capturing *Nat. Genet.* **30** 59–65
- Woodlee R L, Fuh M-R S, Patonay G and Warner I M 1989 Enhanced dc arc lamp performance for spectroscopic applications *Rev. Sci. Instrum.* **60** 3640–2
- Yang C 2005 Molecular contrast optical coherence tomography: a review *Photochem. Photobiol.* **81** 215–37
- Zucker R M, Hunter S and Rogers J M 1998 Confocal laser scanning microscopy of apoptosis in organogenesis-stage mouse embryos *Cytometry* **33** 348–54